Aqueous Batteries

How to cite: *Angew. Chem. Int. Ed.* **2023,** *62,* e202218922
International Edition: doi.org/10.1002/anie.202218922
German Edition: doi.org/10.1002/ange.202218922

NH_4^+ Deprotonation at Interfaces Induced Reversible H_3O^+/NH_4^+ Co-insertion/Extraction

Meng Huang[+], Qiu He[+], Junjun Wang, Xiong Liu, Fangyu Xiong, Yu Liu, Ruiting Guo, Yan Zhao, Jinlong Yang,* and Liqiang Mai**

Abstract: Ion insertions always involve electrode-electrolyte interface process, desolvation for instance, which determines the electrochemical kinetics. However, it's still a challenge to achieve fast ion insertion and investigate ion transformation at interface. Herein, the interface deprotonation of NH_4^+ and the introduced dissociation of H_2O molecules to provide sufficient H_3O^+ to insert into materials' structure for fast energy storages are revealed. Lewis acidic ion-NH_4^+ can, on one hand provide H_3O^+ itself via deprotonation, and on the other hand hydrolyze with H_2O molecules to produce H_3O^+. In situ attenuated total reflection-Fourier transform infrared ray method probed the interface accumulation and deprotonation of NH_4^+, and density functional theory calculations manifested that NH_4^+ tend to thermodynamically adsorb on the surface of monoclinic VO_2, and deprotonate to provide H_3O^+. In addition, the inserted NH_4^+ has a positive effect for stabilizing the VO_2(B) structure. Therefore, high specific capacity ($>300\,mAh\,g^{-1}$) and fast ionic insertion/extraction ($<20\,s$) can be realized in VO_2(B) anode. This interface derivation proposes a new path for designing proton ion insertion/extraction in mild electrolyte.

Introduction

Since the fossil energy has been widely used for hundreds of years, the emission of greenhouse gas CO_2 has produced strongly negative effects on global climate and environment.[1] It is important and urgent to reduce the dependency on fossil energy to improve the health-condition of Earth. Many countries have determined to realize net-zero carbon emissions by the middle of the 21st century.[2] By now, many efforts have been carried out, such as applying solar energy, nuclear energy, wind energy, and reducing the production of fossil-fueled cars, and so forth.[3] Due to the high energy density and long-term cycling performance, lithium-ion batteries (LIBs) have been extensively used to power portable electronic devices and electric vehicles.[4] While endowed high tendency of dendrite formation, the high cost of installation and maintenance, and flammable organic electrolytes render LIBs unsuitable for grid-scale energy storage systems.[5]

Water-based electrolyte batteries, however, are safer and cheaper than LIBs.[6] Although, alkaline rechargeable batteries were invented in 1920s, they are still serving in our daily life because of low cost.[7] Then, mild aqueous electrolyte rechargeable batteries (MARBs) were established in 1994.[8] MARBs succeed the characters from both the organic electrolyte LIBs and alkaline rechargeable batteries, and some MARBs have realized high energy/power density and long-term cycling performances in laboratory test. Owing to the features of low cost, high safety, environmental friendliness, and facile installation and maintenance,

[*] M. Huang,[+] J. Yang
Guangdong Research Center for Interfacial Engineering of Functional Materials, College of Materials Science and Engineering, Shenzhen University
Shenzhen, 518060 (China)
and
College of Physics and Optoelectronic Engineering, Shenzhen University
Shenzhen, 518060 (China)
E-mail: yangjl18@szu.edu.cn

M. Huang,[+] J. Wang, F. Xiong, Y. Liu, R. Guo, L. Mai
State Key Laboratory of Advanced Technology for Materials Synthesis and Processing, Wuhan University of Technology
Wuhan, 430070 (China)
E-mail: mlq518@whut.edu.cn

Q. He,[+] Y. Zhao
College of Materials Science and Engineering, Sichuan University
Chengdu, 610065 (China)
E-mail: yan2000@whut.edu.cn

Y. Zhao
The Institute of Technological Sciences, Wuhan University
Hubei, Wuhan 430072 (China)

X. Liu
School of Materials Science and Engineering, Zhengzhou University
Zhengzhou, 450001 (China)

F. Xiong
Department of Physics, City University of Hong Kong
Tat Chee Avenue, Kowloon, 999077, Hong Kong (China)

Y. Liu
Department of Materials Science and Engineering, National University of Singapore
Singapore, 117574 (Singapore)

[+] These authors contributed equally to this work.

MARBs thus are considered the promising candidates for grid-scale energy storage.[9]

In MARBs, different charge carriers, like H_3O^+, Li^+, Na^+, K^+, NH_4^+, Zn^{2+}, Mg^{2+}, Ca^{2+}, and Al^{3+}, have various radius and hydrated structures, thus show distinct differences in diffusion kinetics in solution.[10] During faradic reaction processes, ions are inserted through tunnels into the host materials.[11] The tunnel size and structure, and the radius of the ion or hydrated ion determine the thermodynamics and kinetics of the insertion/extraction processes. Small ions and large tunnels are certainly beneficial for the insertion/extraction reaction kinetics and thermodynamics.[12] Ions exist in aqueous solution in hydrated states, and most of them will fully or partially dehydrate at electrode-electrolyte interface to have suitable size to insert, slowing down the insertion.[13] Inside the host materials, ions will diffuse along the tunnel to reach their storage sites. This solid-phase diffusion course finally decides the reaction kinetics. Therefore, ions with high charge densities will undergo sluggish dehydration processes before insertion, and obstructed diffusion due to strong electrostatic force from the host materials.

Compared with other hydrated ions, H_3O^+ ions have the smallest radius, the lowest weight, and a higher ionic diffusion, showing strong vitality for aqueous energy storage systems with high energy/power density.[14] Acidic solutions are the commonly used electrolytes for proton batteries. It cannot be ignored that most oxides materials cannot survive in acidic solutions, and it takes much attentions to deal with the exhausted liquid. Compared to H_3O^+, NH_4^+ ions have gained much attentions because of their fast diffusion kinetics in aqueous solutions, small molar mass (18 g mol^{-1}), and abundance.[15] In addition, NH_4^+ is less corrosive than H_3O^+, which is beneficial for storage and transportation. In the present work, derivation of H_3O^+ from NH_4^+ is manifested at the electrode-electrolyte interfaces, causing the co-insertion of H_3O^+ into host materials for fast energy storage.

Herein, we demonstrated that the deprotonation of NH_4^+ and dissociation of H_2O molecules at the electrode-electrolyte interfaces can provide sufficient H_3O^+ for reversible insertion into VO_2 (B, monoclinic phase). In mild aqueous CH_3COONH_4 solution, NH_4^+ acts as charge carriers shuttling from cathode materials to anode electrode-electrolyte interfaces. With continuous accumulation, H_3O^+ can derivate from NH_4^+ for subsequent insertion. Additionally, the co-inserted NH_4^+ ions can stabilize the crystal structure of the host.

Results and Discussion

The sample has a metastable monoclinic crystalline structure of VO_2(B) with a specific layered structure of edge-sharing VO_6 octahedra, and impurity is unobserved (Figure 1a).[16] The Rietveld refinement outcomes are $R_{wp}=5.58\,\%$, $R_p=4.10\,\%$ and $\chi^2=6.436$, with lattice parameters of $a=12.0536$ (0) Å, $b=3.6937(8)$ Å, $c=6.4217(3)$ Å, $\alpha=\gamma=90.00°$, and $\beta=106.92°$ (Table S1) in the space group of $C\,2/m$.[17] Field

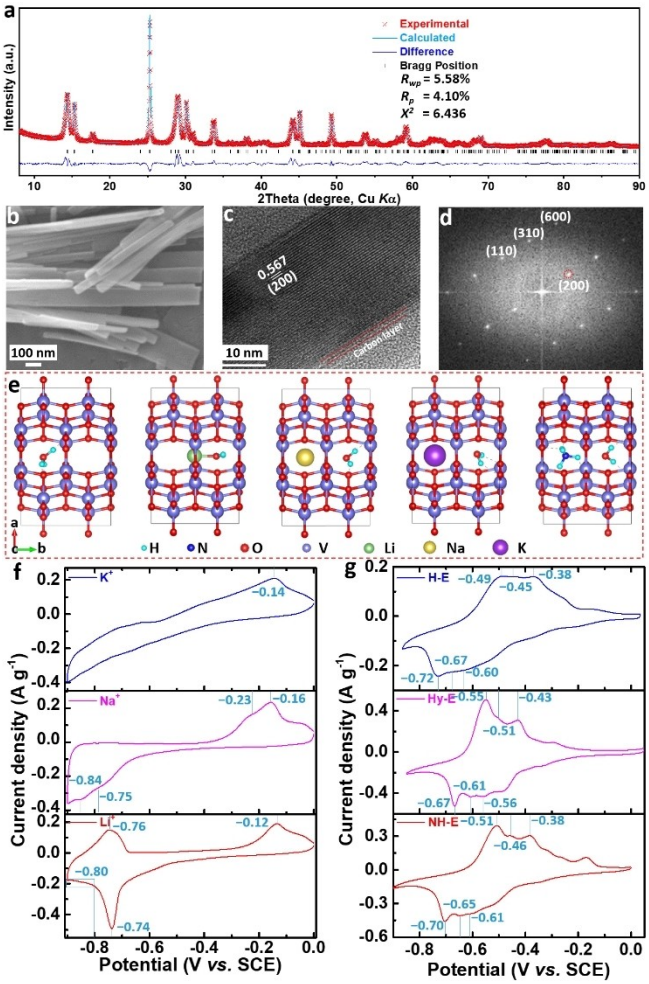

Figure 1. (a) Powder X-ray Rietveld refinement profile for VO_2(B) at 25 °C. (b) SEM image and (c) TEM image of the as-prepared VO_2(B) powder, and (d) is the corresponding fast Fourier transform image. (e) Various VO_2(B) structures with insertion of H_3O^+, Li^+-H_2O, Na^+-H_2O, K^+-H_2O and NH_4^+-H_2O. (f) and (g) CV curves of VO_2(B) in different electrolytes.

emission scanning electron microscopy (FESEM) image shows that the as-prepared sample is composed of nanorods with a diameter of around 100 nm and a length of approximately 1.0 μm (Figure 1b). Transmission electron microscopy (TEM) image manifests that the VO_2(B) nanorod shows an orientated lattice plane of (200) along the longitudinal direction with interlayer spacing of 0.567 nm (Figure 1c).[18] The fast Fourier transform algorithm illustrates only one set of reciprocal lattices, which is in accordance with the (110), (310), (600) and (200) planes of monoclinic phase, indicating that the VO_2(B) nanorod is single crystalline (Figure 1d). The energy-dispersive X-ray spectra (EDS) mappings show the uniform distribution of O and V elements (Figure S1). X-ray photoelectron spectroscopy (XPS) spectrum shows peaks at 516.3 and 517.6 eV, derived from V^{3+} and V^{4+}, respectively, with ratio of 22.9 to 77.1 (Figure S2).[15b] The existence of V^{3+} is due to the formation of oxygen vacancy in the as-prepared VO_2. Infrared (IR) spectrum shows a broad peak at 555 cm^{-1}, and

two sharp peaks at 945 and 1022 cm^{-1}, attributed to V–O vibration, V^{3+}=O streching, and V^{4+}=O streching, respectively (Figure S3).[19] And the peaks at 693 and 812 cm^{-1} corresponde to stretching vibration mode of V–O–V.[19a,20] Thermogravimetric analysis (TGA) shows a weight gain of 7.64 % from 300 to 450 °C, which is due to the oxidation of V^{III} and V^{IV} to V^{V} under air atmosphere (Figure S4). Additionally, the Brunauer–Emmett–Teller (BET) specific surface area is determined to be 27.5 $m^2 g^{-1}$ and stacking pores of 26.5 nm in diameter are observed in Barret-Joyner-Halenda (BJH) pore distribution (Figure S5).

As reported, VO_2(B) has large tunnels of 8.2 $Å^2$ for ion diffusion along the *b*-axis and many sites for ion storage.[21] Through density functional theory (DFT) calculations, H^+ and Li^+ can be inserted into VO_2(B) structure with a hydrated H_2O molecule (Figure 1e). H_3O^+ bonds to O atom in tunnel C site (along c direction) and Li^+ occupies tunnel A site (along b direction). Na^+, K^+, and NH_4^+ can only take the tunnel C site due to their large ion radius. The insertion energy of H_3O^+, Li^+, Na^+, K^+, and NH_4^+ is −2.56, −2.10, −2.78, −2.21 and −2.53 eV, respectively (Table S2). To study the ionic storage behaviors of VO_2(B) in different aqueous electrolytes, including Li_2SO_4 (Li-E), $NaClO_4$ (Na-E), KCF_3SO_3 (K-E), CH_3COOH (H-E), CH_3COOH + CH_3COONH_4 (Hy-E) and CH_3COONH_4 (NH-E) aqueous solution and CH_3COONH_4 in ethylene glycol solution (EG-E), cyclic voltammetry (CV) (Figure 1f and 1g) and galvanostatic discharge/charge tests were applied (Figure S6).

In Li-E electrolyte at a scan rate of 0.1 mV s^{-1}, the CV curve shows two pairs of redox peaks, i.e., −0.8/−0.76 V and −0.74/−0.12 V (vs. saturated calomel electrode (SCE)) (Figure 1f, red curve). Correspondingly, the discharge curve shows two plateaus at −0.12 V and −0.74 V, and one slope below −0.8 V (Figure S6a, magenta curve). Upon charging, one slope below −0.80 V, one plateau at −0.70 V and another plateau at −0.08 V are observed. The redox peaks and charge/discharge plateaus at low potential show fast reaction kinetics, while that at high potentials indicate the poor reaction kinetics. In addition, a specific capacity of ≈168.5 mAh g^{-1} is provided by Li^+ insertion/extraction. In Na-E electrolyte, the CV curve shows two pairs of redox peaks, at −0.75/−0.16 V, and −0.84/−0.23 V, respectively (Figure 1f, magenta curve). The corresponding discharge/charge curves show continuous discharge and charge plateaus, with large potential hysteresis (Figure S6a, blue curve). The large potential hysteresis over 400 mV of these two redox processes mean Na^+ insertion/extraction processes underwent at a poorer rate than that of Li^+. Na^+ insertion/extraction provides a specific capacity of ≈172.1 mAh g^{-1}. For K-E electrolyte, the CV curve shows a slope during the reduction process and a broad oxidation peak at −0.14 V (Figure 1f, blue line), indicating that K^+ are hard to insert into the tunnel structure of VO_2(B). As revealed by the CV results (Figure 1f), alkaline ions show poorer thermodynamics and kinetics in insertion into VO_2-(B) structures with the increasing of ion radius. While in NH-E electrolyte, five pairs of redox peaks, at −0.36/−0.27 V, −0.55/−0.32 V, −0.61/−0.38 V, −0.65/−0.46 V, and −0.70/−0.51 V, respectively, and one solo anodic peak at −0.17 V are observed (Figure 1g, red curve). Corresponding equilibrium potentials for the last three redox peaks are −0.50, −0.56, and −0.61 V, respectively. The first pair redox peaks are small and located on the hillside. The rest peaks overlap and interweave to form the main reduction peak. Upon the oxidation process, relatively small potential hysteresis (≈210 mV) is observed. During the discharge/charge processes, plateaus are overlapped and show small potential hysteresis (Figure S6a, red curve). Small potential hysteresis reveals the faster kinetics of ion insertion/extraction happened in NH-E electrolyte than that in alkaline-ion electrolytes. The continuous redox peaks indicate the complex ion storage processes and a large initial discharge capacity of over 384.5 mAh g^{-1} are achieved. However, NH_4^+ has larger ion radius, and thus the preferred reaction thermodynamics and faster reaction kinetics of VO_2(B) in NH-E electrolyte than in alkaline-ion electrolytes seem to be unreasonable.

To investigate this maze, H-E, Hy-E and EG-E electrolytes were applied. For easy comparison, the potentials of CV curves in H-E and Hy-E have been calibrated to that in NH-E according to the negative correlation between equilibrium potential and pH (Figure S7), and the original ones are enclosed in brackets. In H-E electrolyte, three pairs of calibrated redox peaks at approximately −0.60/−0.38 (−0.30/−0.11), −0.67/−0.45 (−0.40/−0.18) and −0.72/−0.49 (−0.45/−0.22) V are observed, and corresponding equilibrium potentials are −0.49, −0.56, and −0.61 V, respectively, showing high potential hysteresis of over 220 mV (Figure 1g, blue curve). This large capacity is certainly contributed by H_3O^+ insertion and extraction, corresponding to 230 and 217 mAh g^{-1}, respectively (Figure S6b, magenta curve). In Hy-E electrolyte, five pairs of redox peaks at −0.33/−0.30 (−0.23/−0.20 V), −0.49/−0.36 (−0.39/−0.26 V), −0.56/−0.43 (−0.46/−0.33 V), −0.61/−0.51 (−0.51/−0.41 V), and −0.67/−0.55 (−0.57/−0.45 V) show low potential hysteresis of less than 130 mV, and corresponding equilibrium potentials for the last three redox peaks are −0.50, −0.56, and −0.61 V, respectively (Figure 1g, magenta curve). Better reaction kinetics in Hy-E is probably attributed to the elevated concentration of H_3O^+, and the discharge and charge capacities are 279 and 245 mAh g^{-1}, respectively (Figure S6b, red curve). The last three redox peaks, overlapping in the broad redox peak, show negligible difference in equilibrium potential in NH-E, H-E and Hy-E electrolytes. Therefore, these similar redox behaviors found in NH-E, H-E and Hy-E electrolytes and H_3O^+-boosted reaction kinetics in Hy-E electrolyte lead to a reliable proposition that H_3O^+ insertion dominates the capacity contribution in NH-E electrolyte condition. The solo anodic peak at −0.17 V could be attributed to the extraction of NH_4^+ (Figure 1g, red curve). Additionally, CV curve in EG-E electrolyte shows a pair of redox peaks at approximately −0.65/−0.2 V (Figure S8). The broad redox peaks and large potential hysteresis of approximately 450 mV indicate the sluggish ion insertion/extraction processes, probably due to the lack of H_2O (H_2O content is 2370 ppm in EG-E). It is well-known that lower charge density of the ion, dehydration and solo insertion happens

easier.[12b] Additionally, NH_4^+ and H_3O^+ probably form hydrogen bond with O in VO_2, which can enhance the ion diffusion.[22] All in all, these ions can all insert into VO_2 thermodynamically, but their diffusion along the tunnels makes a big difference in the reaction kinetics.

In order to investigate the ionic storage mechanisms of VO_2(B) in different electrolytes, in situ XRD measurements were conducted with Zn metal plate as anode (to provide stable reference potential and sufficient charge transfer). In Li-E electrolyte, the discharge profile shows a slope curve till 0.4 V (vs. Zn^{2+}/Zn), a short plateau between 0.3–0.4 V and a long plateau at 0.3 V (Figure 2a). The (003) diffraction peak first shifts progressively to higher angles in stage I, indicating the lattice shrinkage along the *c* direction (Figure 2b). Meanwhile, the (−601) and (020) diffraction peaks shift to lower angles during the initial discharge processes, indicating lattice expanding along the *a* and *b* directions. At the end of stage I, (003) and (−601) peaks converge. In stage II, (003), (−601), and (601) diffraction peaks start shifting to lower angles because of the lattice expanding, while other diffraction peaks change negligibly. During stage III, (003), (−601), and (601) diffraction peaks shift to higher angles and evolve into lower intensity. The diffraction peaks show negligible changes in stage IV. In Na-E electrolyte, the discharge profile shows two obvious stages (Figure S9a), while the diffraction patterns undergo three stages (Figure S9b). The same shifting mode to Li-E electrolyte happened in stage I and II. However, (003), (−601) and (020) diffraction peaks take stronger shifting, especially in stage II. In stage III, peak shifting takes a slower speed. During the charge process, diffraction patterns shift back in a shorter period both in Li-E and Na-E. These lattice changes reveal the insertion of Li^+/Na^+ into the lattice structures of VO_2(B), and different evolutions of the diffraction patterns mean storage sites for inserted Li^+/Na^+ are different. Additionally, the shorter discharge/charge curves and diffraction pattern shifting in the subsequent electrochemical processes indicate partially reversible insertion/extraction of Li^+/Na^+. In consistence with the CV and GCD curves, a smaller amount of Na^+ can be inserted into VO_2(B) structure, and a much smaller amount of K^+ can inserted (Figure S10). Alkaline ions show poorer thermodynamics in insertion into VO_2(B) structures as the ion radius increases, which is also evidenced by CV results.

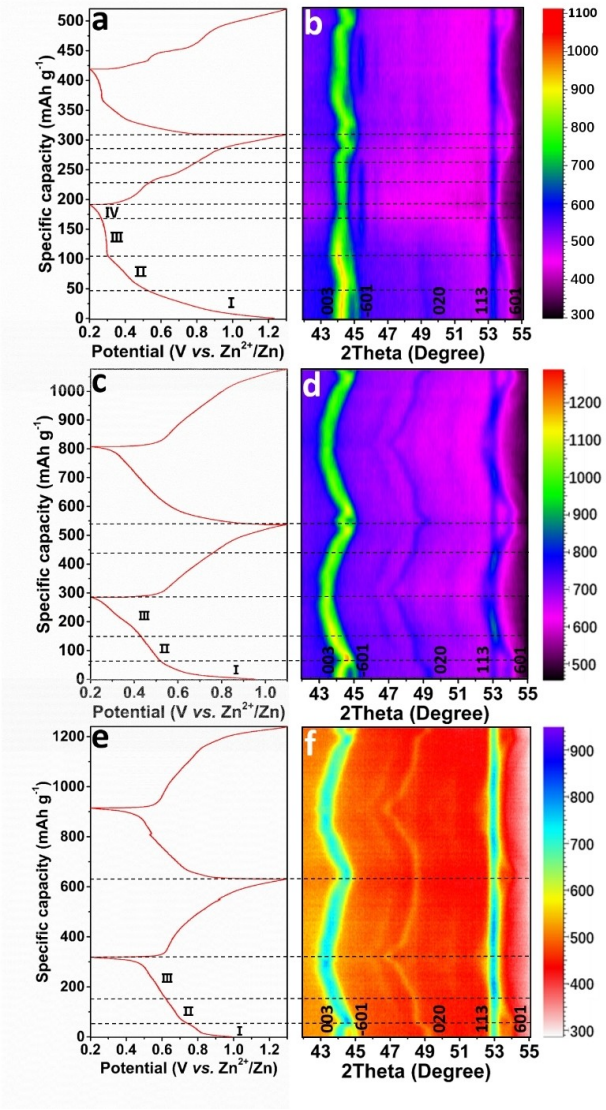

Figure 2. In situ XRD characterizations and corresponding charge/discharge curves of VO_2(B) materials in different electrolytes: (a and b) Li-E, (c and d) NH-E and (e and f) H-E electrolyte using Bruker D8 Discover X-ray diffractometer with a nonmonochromated Cu Kα X-ray source (Power = 1600 W, λ = 1.5418 Å).

In NH-E electrolyte, the discharge profile shows a slope curve till 0.5 V, a short plateau between 0.4–0.5 V and a short slope below 0.4 V (Figure 2c). During stage I, the same shifting mode is observed as in Na-E electrolyte (Figure 2d). In stage II, all the diffraction peaks, except (113), shift to lower angles. After a short period, (601) (113) peaks converge, and subsequently, start shifting to lower angle. Additionally, (003), (−601), and (020) peaks show intensity decay. In stage III, a slower rate shifting of (003) and (−601) peaks is observed. By the end of discharge, (113) and (601) peaks separate from each other. During the charge process, diffraction patterns take the reverse shifting mode. These obvious lattice changes reveal ions insertion into the lattice structures of VO_2(B). Different evolutions of the diffraction patterns are determined by the change of the ion storage sites. Little shorter process and lower intensity in the charge process reveal the partially irreversible insertion/extraction in the first cycle. The subsequent discharge/charge curves and diffraction peak shifting indicate highly reversible insertion/extraction of ion into/from VO_2(B). The lattice expansion extents of (003), (020) and (601) are 1.6 %, 4.1 % and 1.9 %, respectively (Figure S11). The highly similar diffraction evolution model (Figure 2d and 2f) and electrochemical behaviors (Figure 1g) observed in NH-E to that in H-E indicate that H_3O^+ probably dominates the insertion in NH-E, and probably partial NH_4^+ is involved according to the DFT calculations (Figure 1e). Proton insertions have been observed in near-neutral aqueous electrolytes.[23] However, owing to the low concentration (1.0×10^{-7} M) of H_3O^+ in NH-E electrolyte, NH_4^+ at

the electrode-electrolyte interface probably deprotonates to provide sufficient H_3O^+ to insert into VO_2(B) structure. Recently, the insertion of NH_4^+ into vanadium oxides achieved low reversible capacities, which further supports the insertion of H_3O^+ in this work.[10c,15b]

Ex situ TEM and X-ray photoelectron spectra (XPS) measurements were conducted to reveal the structure and valent-state evolution of VO_2(B) in NH-E (Figure S12 and S13). The initial lattice spacing of (200) plane is 0.567 nm (Figure 1c).[24] Two peaks at 517.6 eV and 516.3 eV of XPS spectrum of as-prepared VO_2(B) correspond to V^{4+} (77.1 %) and V^{3+} (22.9 %), respectively (Figure S2).[25] After discharging to −0.5 V and −0.9 V (vs. SCE) at a current density of 150 mA g^{-1}, the lattice spacings of (200) plane increase to 0.579 nm (Figure S12a) and 0.587 nm (Figure S12b), respectively, corresponding to a maximum lattice expanding of 3.5 %. Correspondingly, the ratios of V^{4+} and V^{3+} decrease and increase to 38.2 % and 61.8 %, respectively (Figure S13), which is ascribed to the insertion of ion into VO_2(B) when discharged to −0.9 V. After charging to −0.5 V and 0.0 V, the lattice spacings decrease to 0.576 nm (Figure S12c) and 0.565 nm (Figure S12d), respectively. The lattice spacing of VO_2(B) reverses well, indicating the reversible structure evolution which is consistent with the in situ XRD results (Figure 2c–d).

In order to investigate the interface processes of the reaction, in situ attenuated total reflection-Fourier transform infrared (ATR-FTIR) spectroscopy was applied. To better understand the revolution of peaks in the in situ tests, ATR-FTIR spectra of fresh paste films after soaked in various electrolytes were collected (Figure S14). After soaked in distilled water, Li-E electrolyte and H-E electrolyte, the main peaks below 1700 cm^{-1} are decreased in intensity, while the peaks in the arrangement of 1900–2300 cm^{-1} maintained well. The same extent of decrease in intensity of those peaks below 1700 cm^{-1} are probably caused by the adsorption of H_2O molecules on VO_2(B). On the contrary, NH-E electrolyte cause the formation of downward peaks below 1700 cm^{-1}, which is probably caused by the strongly adsorbed NH_4^+ ions and NH_3 molecules on VO_2(B).[26] In the in situ test, peaks in the range of 1050–1250 cm^{-1} corresponding to symmetric in-plane bending vibration of free NH_3 at low part (orange rectangle) and V-NH_3 (coordinated to Lewis acidic metal atom V) at high part (green rectangle) decrease in intensity (Figure 3a and 3b).[27] Peaks at 1420 and 1460 cm^{-1} attribute to symmetric bending vibration of free NH_4^+ and V-NH_4^+ (coordinated to Lewis acidic metal atom V). Peak at 1540 cm^{-1} due to N–H···O vibration between NH_4^+ and VO_2(B) is also revealed.[28] During the discharge process, the intense increasing of peaks between 1300–1600 cm^{-1} indicates the accumulation of NH_4^+ at the electrode-electrolyte interface, accompanied by the increasing of V-NH_4^+ and N–H···O vibration. The followed appearances of peaks in the range of 1050–1250 cm^{-1} indicate the production of NH_3 at the electrode-electrolyte interface. These vibration peaks be-

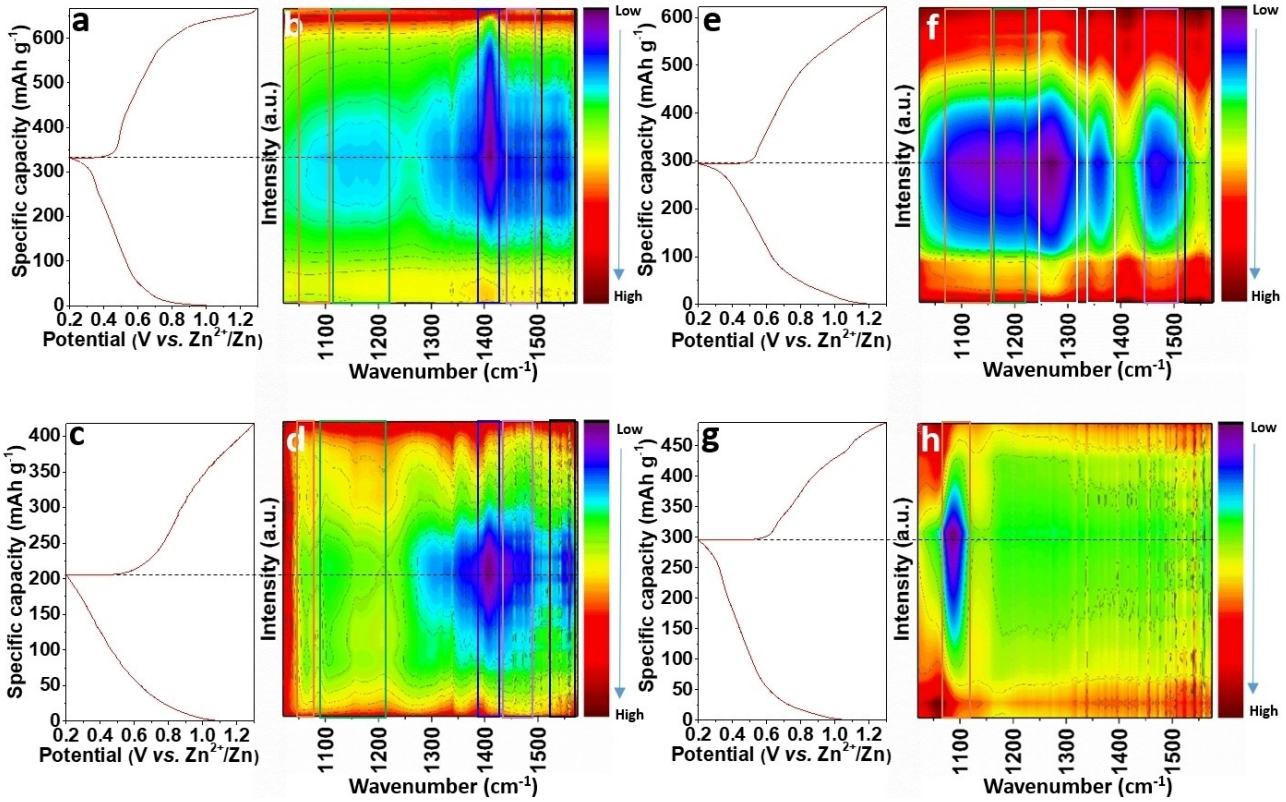

Figure 3. In situ ATR-FTIR characterizations and corresponding charge/discharge curves of VO_2(B) electrodes in different electrolytes: (a and b) NH-E electrolyte, (c and d) EG-E, (e and f) H-E electrolyte, and (g and h) Li-E electrolyte.

tween 1300–1600 cm^{-1} are also observed in EG-E electrolyte (Figure 3c and 3d), but not in H-E electrolyte (Figure 3e and 3f) or Li-E electrolyte (Figure 3g and 3 h). Peaks in the arrangement of 1050–1300 cm^{-1} observed in H-E electrolyte should be originated from the H_3O^+ adsorption on the surface and insertion into the lattice structure of VO_2(B). Likewise, peak evolution at 1090 cm^{-1} observed in Li-E electrolyte should be the adsorption and insertion of Li^+. It should be noticed that the discharge/charge capacity in EG-E is much smaller than that in other electrolytes. The accumulation of NH_4^+ and followed appearance of NH_3 at the electrode-electrolyte interface testify the fact that accumulated NH_4^+ on the surface of VO_2(B) can deprotonate to provide H_3O^+ for insertion/extraction.

DFT simulations have revealed the reaction mechanisms of different cations with the VO_2(B) surface and demonstrated that the deprotonation occurred as the accumulation of NH_4^+ on the VO_2(B) surface. First, the binding energies of different cations on VO_2(B) surface with different coverage rates indicate that NH_4^+ and H_3O^+ ions have higher adsorption energy on the surface of VO_2(B) compared to Li^+, Na^+, K^+, especially in the 2×2-1 and 1×1-1 systems (Figure 4a), and the corresponding structures are shown in Figure S15 and 4b. Focusing on the structure evolution of NH_4^+ as the increase of the concentration of adsorbed NH_4^+, the deprotonation process of NH_4^+ can be easily observed. In details, in a 2×2-1 system with low concentration of NH_4^+, intact NH_4^+ is adsorbed on the surface via H-bonding (Figure 4b). Increasing the ratio of NH_4^+ as in 1×1-1 and 1×1-2 system, H^+ is released from NH_4^+ and deprived by the adjacent O atom of VO_2(B) surface. Despite the strong attraction of VO_2(B) surface to NH_4^+, driven by the electric field force during the discharge processes, NH_4^+ continuously diffuses to and accumulates at the electrode-electrolyte interface. As a result, a NH_4^+-rich domain is formed, which is probed by the in situ FTIR (Figure 3b), to provide enough reaction thermodynamics and kinetics for NH_4^+ deprotonation. Additionally, it is well known that NH_4^+ is a kind of Lewis acid, and the hydrolysis formula of NH_4^+ as follows

$$NH_4^+ + 2H_2O \leftrightarrow NH_3 \cdot H_2O + H_3O^+ \quad (1)$$

is an endothermic reaction with the calculated free energy of 39.93 kcal mol^{-1} in implicit water environment at 298.15 K.[29] By contrast, the free energy of the hydrolysis of water, i.e.,

$$2H_2O \leftrightarrow HO^- + H_3O^+ \quad (2)$$

is 74.53 kcal mol^{-1}. The smaller reaction free energy implies that Equation (1) happens thermodynamically prior to Equation (2), which indicates that the deprotonation of NH_4^+ probably dominates the formation of H_3O^+. The much lesser discharge capacity in EG-E supports that H_2O also plays an indispensable role (Figure 3c). Thus, H_2O can boot the deprotonation of NH_4^+. The derived H_3O^+ can be also easily adsorbed on the surface of VO_2(B) (Figure 4a). Ion diffusion strongly determines the reaction processes, including surface diffusion and inside diffusion. As for the surface diffusion, NH_4^+ shows little lower energy barriers by 0.24 eV than proton (Figure 4c). However, in the tunnel structure, proton has much lower diffusion energy barrier of 0.52 eV (Figure 4d). At the NH_4^+-inserted VO_2(B) structure, proton has a little higher diffusion energy barrier of 0.88 eV, indicating that the inserted NH_4^+ show little obstruction for proton diffusion. Therefore, surface diffusion and interface deprotonation of NH_4^+ decide the insertion reaction kinetics, which is consistent with the CV, in situ XRD and in situ FTIR results. After insertion, proton prefers the sites adjacent to O atoms, and O5 site has relatively the lowest storage energy for proton (Figure S16). When the tunnel sites are occupied by the inserted NH_4^+, the subsequent inserted proton would prefer O4 sites (Figure 4e, S17). According to our analysis, a reaction mechanism of interface deprotonation of NH_4^+ to provide H_3O^+ for the subsequent insertion is confirmed and verifies the aforementioned proposition (Figure 4e).

According to the aforementioned results and analysis, H_3O^+ and NH_4^+ are co-inserted into VO_2(B) lattice structure and provide reversible specific capacity of over 300 mAh g^{-1}. Additionally, the ionic conductivity of NH-E is much higher than that of Li-E (Table S3). As expected,

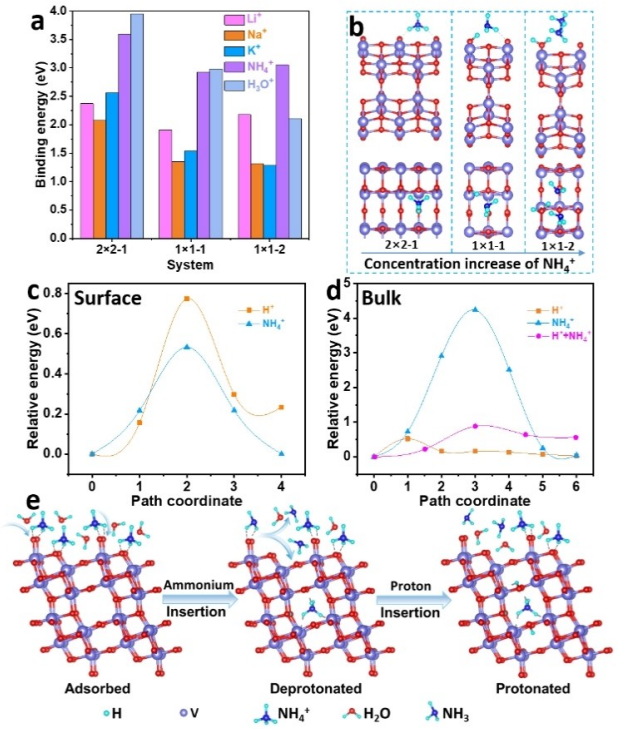

Figure 4. (a) Binding energies of Li^+, Na^+, K^+, NH_4^+ and H_3O^+ on VO_2(B) surface with different coverage rates (2×2-1 means one cation on a 2×2 supercell). (b) Optimized adsorption structures of one NH_4^+, one NH_4^+, and two NH_4^+ on 2×2, 1×1, and 1×1 supercells of VO_2(B) surface, respectively. (c) Diffusion energy barrier of H_3O^+, NH_4^+ on VO_2(B) surface. (d) Diffusion energy barrier of H_3O^+, NH_4^+, and $H_3O^+ + NH_4^+$ inside VO_2(B) bulk. (e) Schematic diagram of the deprotonation processes on VO_2(B) surface and synergetic ionic storage mechanism of H_3O^+-NH_4^+.

VO_2(B) has much better rate capability in NH-E than in Li-E (Figure 5a and S18). The discharge capacities of VO_2(B) in NH-E at 0.5, 1.0, 2.0, 3.0, 5.0, 10.0, 20.0 and 30.0 A g^{-1} are 385, 337, 303, 283, 253, 194 and 117 mAh g^{-1}, respectively, and those are 210, 177, 169, 126, 95, 81 and 64 mAh g^{-1}, respectively, in Li-E. Although the ionic conductivity has few differences between Hy-E and NH-E, the lower capability of in Hy-E is probably caused by the instability of VO_2(B) in acid solution (Table S4). In comparison, the high-rate capability of ion insertion can be achieved in NH-E. At a current density of 10 A g^{-1} in NH-E, the initial discharge capacity of VO_2(B) is 270.33 mAh g^{-1} and the second discharge capacity is 191.2 mAh g^{-1} (Figure 5b). The Coulombic efficiency is as high as ≈99 %. After cycling for 1000 cycles, the capacity is 150.3 mAh g^{-1}. In Hy-E, the first and second discharge capacity is 204 and 165 mAh g^{-1}, respectively. After 1000 times cycling, only 65 mAh g^{-1} is left. Thus, it can be found that a little higher H_3O^+ concentration provided by Hy-E is a double-edged sword, which can both ensure fast insertion kinetics and dissolve VO_2(B), which is magnified in the cycling test. By contrast, NH_4^+ deprotonation at the electrode-electrolyte interface providing sufficient H_3O^+ to insert into VO_2(B) structure is a better path for highly reversible H_3O^+ insertion/extraction. In Li-E, the first and second discharge capacities are 165 and 143 mAh g^{-1}, respectively. After 986 times cycling, a capacity of 60 mAh g^{-1} is left, which is caused by irreversible Li-extraction revealed by in situ XRD, and a low Coulombic efficiency of ≈98 % is obtained. At a higher current density of 20 A g^{-1} in NH-E, the second discharge capacity of 107.5 mAh g^{-1} is obtained, and after 5000 cycles, 61.2 % of that is maintained (Figure S19). CVs at different scanning rates in the range of 0.1–5.0 mV s^{-1} are displayed in Figure S20. The potential hysteresis of main peak increases from 50 mV at 0.1 mV s^{-1} to 150 mV at 5.0 mV s^{-1}. Capacitive-controlled capacity dominates 61 %, 67 %, 75 %, 77 %, and 83 % at 0.2, 0.4, 0.8, 1.0, and 2.0 mV s^{-1}, respectively (Figure S21). The fast pseudocapacitance of VO_2(B) in NH-

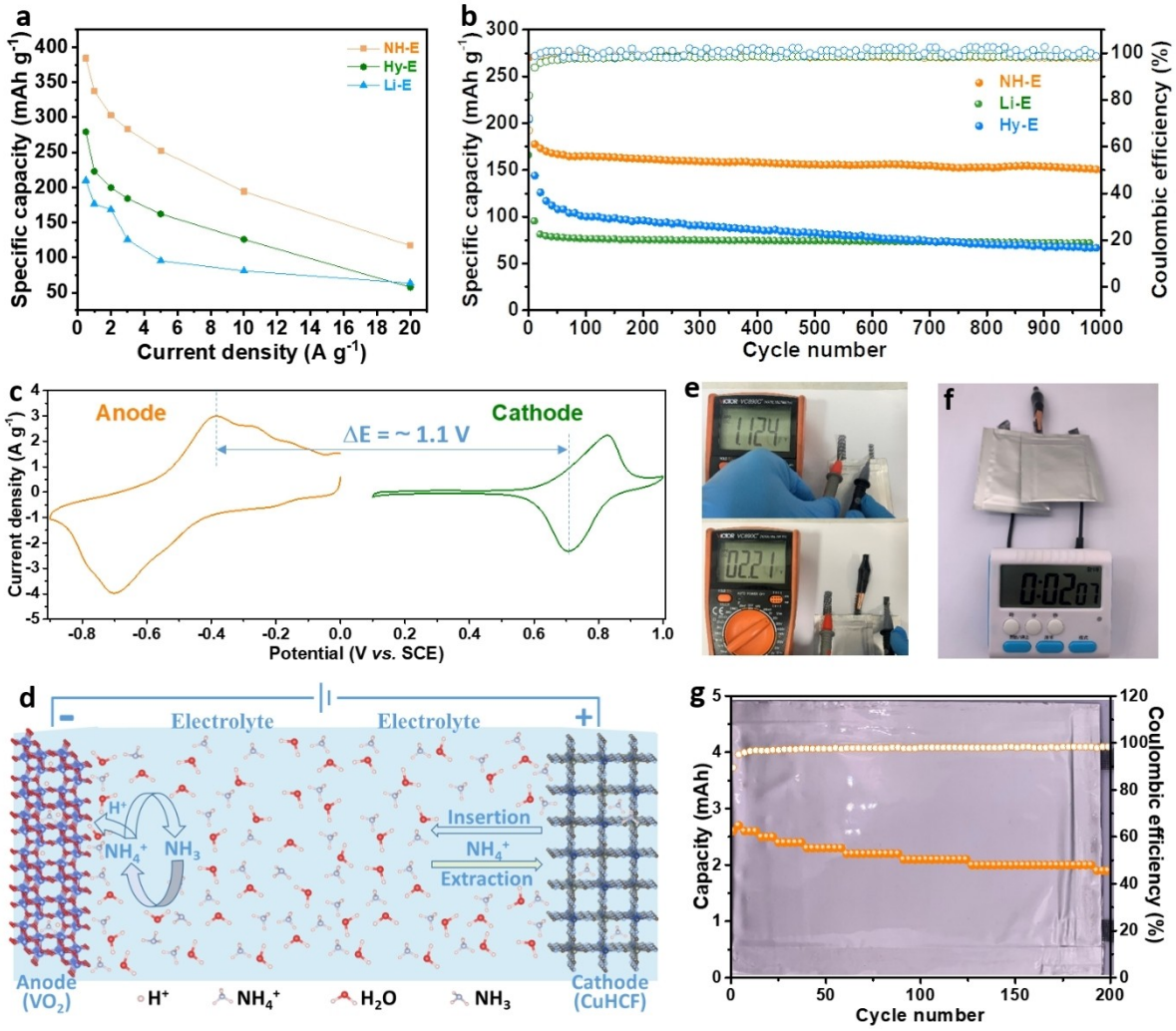

Figure 5. (a) Rate capability (b) cycling performance at a current density of 10 A g^{-1} of VO_2(B) electrodes at different electrolytes. (c) CV curves of VO_2(B) and $(NH_4)_2CuFe(CN)_6$ electrodes at 2.0 mV s^{-1}. (d) The working scheme of aqueous VO_2(B)//$(NH_4)_2CuFe(CN)_6$ battery system. (e) Open circuit potentials of one pouch cell and two pouch cells in series. (f) One powered time counter by two pouch cells in series. (g) Cycling performance at 3.0 A g^{-1} of VO_2(B)//$(NH_4)_2CuFe(CN)_6$ pouch cell.

E is promising for high energy/power density energy storages. The ion diffusion coefficients are calculated by galvanostatic intermittent titration technique (GITT) to be in the range of 10^{-10}–10^{-8} $cm^2 s^{-1}$ (Figure S22), which attributes to the fast ion storage features of VO_2(B) in NH-E.[30] Based on the CV curves of VO_2(B) and $(NH_4)_2CuFe(CN)_6$ (Figure S23 and S24, Table S5 and S6, as cathode materials) at 2.0 $mV s^{-1}$, a discharge plateau at ≈1.1 V of the full cell is expected (Figure 5c), which is consistent with the pair of redox peaks of 1.12/1.53 V of the full battery (Figure S25). Therefore, a full cell based on NH_4^+-deprotonating insertion into VO_2(B) anode and NH_4^+ insertion into $(NH_4)_2CuFe(CN)_6$ can be assembled (Figure 5d).[31] When cycled at a current density of 5.0 $A g^{-1}$, the full battery (mass ratio of VO_2(B): $(NH_4)_2CuFe(CN)_6$ is 1:6.7) shows a capacity retention of 62.0 % (Figure S26). For realistic applications, VO_2(B)//$(NH_4)_2CuFe(CN)_6$ pouch cells are also constructed at the active mass ratio of 1:6. Single pouch cell has an open circuit potential of 1.1 V, and 2.2 V for two in series (Figure 5e). Two in series can power a time counter (Figure 5f). The pouch cell shows an initial capacity of 2.7 mAh, and 70.3 % of that is maintained after 200 cycles at a current density of 3 $A g^{-1}$ (based on anode mass) (Figure 5g). Thus, the NH_4^+ deprotonation for reversible H_3O^+ insertion/extraction is promising for energy storage.

Conclusion

We have shown that the accumulated NH_4^+ ions at the electrode-electrolyte interface can deprotonate to produce H_3O^+ for reversible insertion into VO_2(B) by in situ ATR-FTIR and DFT calculations. In addition, Lewis acidic ion-NH_4^+ can hydrolyze with H_2O molecules to produce H_3O^+ spontaneously when they are accumulated at the surface of VO_2(B). The NH_4^+ itself shuttles from cathode materials to anode electrode-electrolyte interfaces acting as charge carriers. The co-inserted NH_4^+ ions stabilize the crystal structure of the host for better cycling performance compared to the acidic electrolyte. Therefore, high specific capacity (>300 mAh g^{-1}), and fast ionic insertion/extraction (<20 s) can be realized in VO_2(B) anode (≈0.5 vs. SCE). This interface derivation proposes a new path for designing proton insertion/extraction.

Acknowledgements

This work was financially supported by the Natural Science Foundation of Guangdong Province (No.2021A1515010144), the National Key Research and Development Program of China (Grant No. 2020YFA0715000), and the National Natural Science Foundation of China (Grant No. 52127816 and No. 51832004).

Conflict of Interest

The authors declare no conflict of interest.

Data Availability Statement

The data that support the findings of this study are available from the corresponding author upon reasonable request.

Keywords: Electrode-Electrolyte Interface · Energy Storage Mechanism · Proton Insertion · Vanadium Dioxide · In Situ Characterization

[1] X. Huang, Y.-B. Zhang, *Coord. Chem. Rev.* **2021**, *427*, 213564.
[2] N. Jennings, M. Rao, *BMJ* **2020**, *371*, m3884.
[3] a) H. Zsiborács, N. H. Baranyai, A. Vincze, L. Zentkó, Z. Birkner, K. Máté, G. Pintér, *Electronics* **2019**, *8*, 729; b) R. T. Timakova, R. V. Iliukhin, I. V. Iliukhina, *IOP Conf. Ser.: Earth Environ. Sci.* **2022**, *979*, 012172.
[4] J. Xie, Y. C. Lu, *Nat. Commun.* **2020**, *11*, 2499.
[5] Y. Kim, G. T. Kim, S. Jeong, X. W. Dou, C. X. Geng, Y. Kim, S. Passerini, *Energy Storage Mater.* **2019**, *16*, 56–64.
[6] a) X. Dong, L. Chen, J. Liu, S. Haller, Y. Wang, Y. Xia, *Sci. Adv.* **2016**, *2*, e1501038; b) H. Zhang, X. Liu, H. Li, I. Hasa, S. Passerini, *Angew. Chem. Int. Ed.* **2021**, *60*, 598-616.
[7] M. Huang, M. Li, C. Niu, Q. Li, L. Mai, *Adv. Funct. Mater.* **2019**, *29*, 1807847.
[8] W. Li, J. R. Dahn, D. S. Wainwright, *Science* **1994**, *264*, 1115–1118.
[9] X. Dong, L. Chen, X. Su, Y. Wang, Y. Xia, *Angew. Chem. Int. Ed.* **2016**, *55*, 7474–7477.
[10] a) M. Huang, X. Wang, X. Liu, L. Mai, *Adv. Mater.* **2022**, *34*, 2105611; b) H. Zhang, X. Li, J. Hou, L. Jiang, H. Wang, *Chem. Soc. Rev.* **2022**, *51*, 2224–2254; c) D. Yu, Z. Wei, X. Zhang, Y. Zeng, C. Wang, G. Chen, Z. X. Shen, F. Du, *Adv. Funct. Mater.* **2021**, *31*, 2008743.
[11] D. Chao, H. J. Fan, *Chem* **2019**, *5*, 1359–1361.
[12] a) C. Ling, J. J. Chen, F. Mizuno, *J. Phys. Chem. C* **2013**, *117*, 21158–21165; b) S. Phadke, R. Mysyk, M. Anouti, *J. Energy Chem.* **2020**, *40*, 31–38; c) Z. Wei, W. Shin, H. Jiang, X. Wu, W. F. Stickle, G. Chen, J. Lu, P. Alex Greaney, F. Du, X. Ji, *Nat. Commun.* **2019**, *10*, 3227.
[13] L. Chen, H. Shao, X. Zhou, G. Liu, J. Jiang, Z. Liu, *Nat. Commun.* **2016**, *7*, 11982.
[14] G. Liang, F. Mo, X. Ji, C. Zhi, *Nat. Rev. Mater.* **2021**, *6*, 109–123.
[15] a) J. Han, A. Varzi, S. Passerini, *Angew. Chem. Int. Ed.* **2022**, *61*, e202115046; *Angew. Chem.* **2022**, *134*, e202115046; b) Y. Wu, S. Dong, N. Lv, Z. Xu, R. Ren, G. Zhu, B. Huang, Y. Zhang, X. Dong, *Small* **2022**, *18*, 2204888.
[16] L. Chen, Y. Ruan, G. Zhang, Q. Wei, Y. Jiang, T. Xiong, P. He, W. Yang, M. Yan, Q. An, L. Mai, *Chem. Mater.* **2019**, *31*, 699–706.
[17] F. Izumi, K. Momma, *Solid State Phenom.* **2007**, *130*, 15–20.
[18] C. Niu, J. Meng, C. Han, K. Zhao, M. Yan, L. Mai, *Nano Lett.* **2014**, *14*, 2873–2878.
[19] a) I. L. Botto, M. B. Vassallo, E. J. Baran, G. Minelli, *Mater. Chem. Phys.* **1997**, *50*, 267–270; b) V. S. R. Channu, R. Holze, B. Rambabu, *Curr. Appl. Phys.* **2013**, *13*, 237–240.
[20] Y. Shimizu, K. Nagase, N. Miura, N. Yamazoe, *J. Appl. Phys.* **1990**, *29*, L1708–L1711.
[21] Q. Liu, G. Tan, P. Wang, S. C. Abeyweera, D. Zhang, Y. Rong, Y. A. Wu, J. Lu, C.-J. Sun, Y. Ren, Y. Liu, R. T. Muehleisen, L. B. Guzowski, J. Li, X. Xiao, Y. Sun, *Nano Energy* **2017**, *36*, 197–205.
[22] a) G. Liang, Y. Wang, Z. Huang, F. Mo, X. Li, Q. Yang, D. Wang, H. Li, S. Chen, C. Zhi, *Adv. Mater.* **2020**, *32*, 1907802; b) S. Y. Dong, W. Shin, H. Jiang, X. Y. Wu, Z. F. Li, J.

Holoubek, W. F. Stickle, B. Key, C. Liu, J. Lu, P. A. Greaney, X. G. Zhang, X. L. Ji, *Chem-Us* **2019**, *5*, 1537–1551.
[23] a) N. Makivić, K. D. Harris, J.-M. Tarascon, B. Limoges, V. Balland, *Adv. Energy Mater.* **2023**, *13*, 2203122; b) C. Geng, T. Sun, Z. Wang, J. M. Wu, Y. J. Gu, H. Kobayashi, P. Yang, J. Hai, W. Wen, *Nano Lett.* **2021**, *21*, 7021–7029.
[24] X. Xia, D. Chao, C. F. Ng, J. Lin, Z. Fan, H. Zhang, Z. X. Shen, H. J. Fan, *Mater. Horiz.* **2015**, *2*, 237–244.
[25] C. Xia, Z. Lin, Y. Zhou, C. Zhao, H. Liang, P. Rozier, Z. Wang, H. N. Alshareef, *Adv. Mater.* **2018**, *30*, 1803594.
[26] G. A. Blomfield, L. H. Little, *J. Catal.* **1971**, *21*, 149–158.
[27] S. Suganuma, Y. Murakami, J. Ohyama, T. Torikai, K. Okumura, N. Katada, *Catal. Lett.* **2015**, *145*, 1904–1912.
[28] S. Wang, Z. Yuan, X. Zhang, S. Bi, Z. Zhou, J. Tian, Q. Zhang, Z. Niu, *Angew. Chem. Int. Ed.* **2021**, *60*, 7056–7060; *Angew. Chem.* **2021**, *133*, 7132–7136.
[29] a) A. Slesinski, C. Matei-Ghimbeu, K. Fic, F. Béguin, E. Frackowiak, *Carbon* **2018**, *129*, 758–765; b) B. Delley, *J. Chem. Phys.* **2000**, *113*, 7756–7764; c) Y. Zhao, D. G. Truhlar, *Theor. Chem. Acc.* **2008**, *120*, 215–241.
[30] W. Weppner, R. A. Huggins, *J. Electrochem. Soc.* **1977**, *124*, 1569.
[31] C. Y. Li, J. H. Wu, F. X. Ma, Y. H. Chen, L. J. Fu, Y. S. Zhu, Y. Zhang, P. Wang, Y. P. Wu, W. Huang, *ACS Appl. Energy Mater.* **2019**, *2*, 6984–6989.

Manuscript received: December 21, 2022
Accepted manuscript online: February 3, 2023
Version of record online: February 21, 2023